

# Precipitates on Granular Iron in Solutions Containing Calcium Carbonate with Trichloroethene and Hexavalent Chromium

SUNG-WOOK JEEN,<sup>†</sup> JOHN L. JAMBOR,<sup>‡</sup> DAVID W. BLOWES,<sup>†,\*</sup> AND ROBERT W. GILLHAM<sup>†</sup>

Department of Earth Sciences, University of Waterloo, Waterloo, Ontario, Canada N2L 3G1, and Leslie Research and Consulting, Tsawwassen, British Columbia, Canada V4M 3L9

Mineralogical examination, using scanning electron microscopy (SEM), X-ray diffractometry (XRD), and optical microscopy, was conducted on the Fe<sup>0</sup>-bearing reactive materials derived from long-term column experiments undertaken to assess the treatment capacity of Fe<sup>0</sup> under different geochemical conditions. The columns received either deionized water or solutions of differing dissolved calcium carbonate concentrations, together either with trichloroethene (TCE) or hexavalent chromium (Cr(VI)). The major reaction product in the columns receiving deionized water was magnetite–maghemite, and for the columns receiving dissolved calcium carbonate, the main products were iron hydroxy carbonate and aragonite. Replacement of Fe<sup>0</sup> by reaction products occurred mainly at the edges of the Fe<sup>0</sup> particles, and penetrative replacement was focused along cracks and along and around graphitic inclusions. Fibrous or flake-shaped iron hydroxy carbonate mostly replaced the edges of the Fe<sup>0</sup> particles. Aragonite had needle-shaped morphology, and some occurred as clusters of crystals. Aragonite was deposited on iron hydroxy carbonate, thus providing at least a partial armoring effect. The mineral was also observed to cement groups of Fe<sup>0</sup> particles into compact aggregates. The Cr was present mostly as Cr(III) in Cr(III)-Fe(III) (oxy)hydroxides and in trace amounts in iron hydroxy carbonate.

## Introduction

In permeable reactive barriers (PRBs) containing Fe<sup>0</sup> as the reactive medium, mineral precipitation varies broadly because of differing geochemical conditions (1). Major mineral phases identified in such PRBs include various iron oxides, hydroxides, and oxyhydroxides, intermediate products (green rusts), carbonates, and iron sulfides (2). In particular, carbonate minerals have been most commonly observed in the PRBs subjected to carbonate-containing groundwater, and the precipitates have been shown to greatly affect the performance of the Fe<sup>0</sup> (3, 4). There have been numerous reports of accumulations of the calcium carbonate minerals, aragonite and calcite (2). Although siderite [FeCO<sub>3</sub>] has often been proposed as a possible iron carbonate phase (5), the

existence of other iron carbonate phases, such as iron hydroxy carbonate [Fe<sub>2</sub>(OH)<sub>2</sub>(CO<sub>3</sub>)], generally has been overlooked (6) and only recently has been considered (7–9).

Mineralogical studies, combined with aqueous analyses, are integral parts of environmental models. Chemical equilibrium and reactive transport models rely on the correct identification and assignment of thermodynamic properties of mineral phases (10, 11). If predictive models are to be useful, these models must be constrained by the specification of mineral phases identified by direct observations (12).

A mineralogical study was conducted as an integral part of a long-term column study (13, 14), which assessed the longevity of Fe<sup>0</sup> treating trichloroethene (TCE) or hexavalent chromium (Cr(VI)) under differing geochemical conditions. The secondary phases were identified, and the characteristics of the reaction products were determined. Emphasis was on determining the morphology and importance of carbonate minerals, including iron hydroxy carbonate. Temporal and spatial variations in mineral assemblages were also investigated. The mineralogical characterization was conducted using scanning electron microscopy (SEM) with energy-dispersion spectroscopy (EDS), X-ray diffractometry (XRD), and optical microscopy.

## Experimental Section

**Column Experiments.** Six columns were assembled to simulate groundwater flow through Fe<sup>0</sup>-bearing PRBs. The extent of formation of carbonate minerals was assessed by passing solutions of differing concentrations of dissolved calcium carbonate through columns containing commercially sourced Fe<sup>0</sup> (Connelly-GPM; Chicago, IL). Columns received 10 mg/L TCE or 10 mg/L Cr(VI) either in deionized water or in solutions containing dissolved calcium carbonate (TCE for columns A–D and Cr(VI) for columns I and II; see Table 1). Grain size was 0.30–2.38 mm in column C and was 0.17–1.41 mm in the other columns. For mineral examination, sampling ports of stainless steel plugs having an outer diameter of 1.27 cm were screwed into the wall of each column (50 cm long and 2.54 cm I.D.). The port locations and scheme of the sampling procedures are provided in Table 1. The columns were operated for about 2 years. Details of the column experiments can be found in Jeen et al. (13, 14).

**Sample Preparation.** Sampling of the Fe<sup>0</sup> materials was performed during operation of the columns on day 250, day 405, day 541, and day 649. For sampling, only a small amount of Fe<sup>0</sup> was taken from each of the selected ports. Different ports were chosen at each sampling event to minimize disturbance of the columns.

Sampling was conducted in a collapsible glove bag under a stream of nitrogen gas because minerals such as green rust are unstable and oxidize rapidly when exposed to O<sub>2</sub> (15). After the sampling port was opened, a small amount of Fe<sup>0</sup> was extracted with a stainless steel spatula and was transferred to a 20 mL plastic vial. For SEM examination of the day 250 sample, the grains were mounted on a specimen stub (with double-sided adhesive tape), and the specimen stub was transferred to a plastic vial. The accumulated plastic vials were placed in an anaerobic canister, sealed with vacuum grease, and the canister was shipped for further analyses. At the last sampling event (on day 649), samples were immersed in alcohol in 20 mL glass vials.

**Scanning Electron Microscopy.** Most of the SEM analyses were conducted on samples collected on day 250. The specimen stub, stored in a plastic vial, was frozen with liquid nitrogen and stored in a freezer for 1 day before analyses. The specimen was coated with gold (10 nm) using a vacuum

\* Corresponding author phone: (519)888-4878; fax: (519)746-3882; e-mail: blowes@sciborg.uwaterloo.ca.

<sup>†</sup> University of Waterloo.

<sup>‡</sup> Leslie Research and Consulting.

**TABLE 1. Location of the Sampling Ports for Each Column and Sampling Scheme on day 250, day 405, day 541, and day 649<sup>a</sup>**

sampling time	column						sample preparation
	A: D.I. H <sub>2</sub> O + 10 mg/L TCE	B: 100 mg/L CaCO <sub>3</sub> + 10 mg/L TCE	C: 100 mg/L CaCO <sub>3</sub> + 10 mg/L TCE, coarse <sup>b</sup> Fe <sup>0</sup>	D: 500 mg/L CaCO <sub>3</sub> + 10 mg/L TCE	I: D.I. H <sub>2</sub> O + 10 mg/L Cr(VI)	II: 500 mg/L CaCO <sub>3</sub> + 10 mg/L Cr(VI)	
day 250	2	2/8/10	2/9	2	2/10	2/10	SEM
day 405		6					SEM/XRD
day 541	4	4	3	4	4	4	XRD/optical microscopy
day 649	5	5	4	5	5	5	XRD

<sup>a</sup> Numbers inside the table represent the numbers of the sampling ports. The location of each sampling port is as follows: For columns A, B, D, I, and II: 1 (3.75 cm), 2 (6.25 cm), 3 (8.75 cm), 4 (12.5 cm), 5 (17.5 cm), 6 (22.5 cm), 7 (27.5 cm), 8 (32.5 cm), 9 (37.5 cm), and 10 (42.5 cm). For column C: 1 (3.75 cm), 2 (7.5 cm), 3 (12.5 cm), 4 (17.5 cm), 5 (22.5 cm), 6 (27.5 cm), 7 (32.5 cm), 8 (37.5 cm), and 9 (42.5 cm). <sup>b</sup> Grain size is 0.30–2.38 mm and is 0.17–1.41 mm in the other columns. <sup>c</sup> Distance from the influent end of the column.

evaporator. A specimen of the Fe<sup>0</sup> used in the column experiments, as received from the supplier, was prepared using the same procedure. SEM images were acquired at 15 kV using a LEO 1530 field emission scanning electron microscope (FE-SEM). EDS analyses were obtained at 15 kV using a EDAX Pegasus 1200 integrated EDX/OIM system, attached to the FE-SEM. On day 405, a sample from column B was analyzed (Table 1). The extracted Fe<sup>0</sup> sample, stored in a N<sub>2</sub> gas-filled 20 mL plastic vial, was shipped inside the anaerobic canister, and the mount of the grains on a specimen stub was made after the shipment. The sample material was carbon-coated and examined using a Philips XL-30 SEM with a Princeton Gamma Tech energy-dispersion analyzer.

**X-ray Diffraction and Optical Microscopy.** Samples taken on day 405 and day 541 were used for examination by XRD and optical microscopy. Immediately after the anaerobic canister and vial were opened, the contents were emptied into a mortar and immersed in alcohol prior to transferring the unground sample to a zero-background plate for X-ray diffractometry. Diffractograms were obtained using a Siemens rotating-anode diffractometer and Cu K $\alpha$  X-radiation. The sample was rapidly scanned (17 min total) from 6° to 47° 2 $\theta$ , which is a range sufficient to include the major X-ray peaks known or possibly expected to be generated from the column materials. When the full scan was completed for the sample from column B taken on day 405, the sample was immersed in alcohol, and was ground using a mortar and pestle. The fines were periodically decanted and were used for a new diffractogram that was obtained the next day at a step time of 2 s rather than the initial rapid scan at a step time of 1 s. For the sample from column A on day 541, in which the presence of green rust was suspected, upon completion of the initial X-ray scans, for which the total elapsed time including preparation of the X-ray mounts was about 3 h, the same sample was remounted and rescanned to determine whether the original mineralogy had changed.

The samples taken on day 649 had been immersed in alcohol in glass vials in which air space was minimized, rather than using an anaerobic canister for transportation. This set of samples was ground in alcohol with a mortar and pestle, and the resulting fines were decanted into smaller bottles to provide five of the six X-ray samples. The mixture of alcohol and sample was swirled prior to decanting in order to maximize the uptake of fines. The fines were allowed to settle, and subsequently most of the excess clear alcohol was decanted. The exception to this procedure was the sample from column A, whose excess alcohol was gradually removed while the undisturbed solids remained immersed. The grind-and-decant procedure for that sample was implemented immediately prior to the X-ray run. An X-ray mount of the as-received, nonreacted granular Fe<sup>0</sup> was also prepared using the same grind-and-decant procedure.

For the examination by optical microscopy, the material recovered from the X-ray study on day 541 was allowed to

dry at room temperature in ambient atmosphere. The sample materials were submitted to Vancouver Petrographics Ltd. (Langley, BC, Canada) for standard 26  $\times$  46 mm polished thin sections, which were prepared without the use of water. A split of the as-received granular Fe<sup>0</sup> was also submitted for a polished section.

## Results and Discussion

**Visual Observations.** In the columns receiving solutions of dissolved calcium carbonate, mineral precipitation was visually distinguishable as gray or bluish gray reaction fronts. The grayish minerals were thought to be either calcium carbonate or iron carbonate, or both. The progress of the moving front was faster in columns D and II, which were receiving the higher concentrations of dissolved calcium carbonate. In all cases, the precipitation fronts eventually spread throughout the columns because mineral precipitation led to a progressive loss of reactivity of the Fe<sup>0</sup> over time. Details of the behavior of the moving fronts of secondary minerals, consistent with the trends of the pH, Eh, and aqueous concentrations, are given by Jeen et al. (13, 14). Briefly, the pH increase resulting from iron corrosion (> pH 9) was buffered by carbonate precipitation near the influent end of the column at early times, but the pH profiles eventually became almost constant throughout the column because of passivation of the iron. The Eh values increased over time, reflecting the decreased reactivity of the iron. The TCE and Cr(VI) profiles migrated over time. The TCE was transformed mainly to chlorinated intermediates and non-chlorinated hydrocarbons (e.g., ethene and ethane).

For the columns receiving Cr(VI), a brownish precipitation front was observed. In earlier studies, the brownish precipitate was considered to be mixed Fe(III)-Cr(III) (oxy)hydroxide (16). In column II, receiving 500 mg/L CaCO<sub>3</sub> and 10 mg/L Cr(VI), a brownish precipitation front was observed in addition to the grayish carbonate precipitation front. The progress of the grayish precipitation front was much faster than that of the brownish front.

**X-ray Diffraction.** The X-ray diffractogram of the decanted fines from the as-received iron showed that the most abundant minerals were magnetite [Fe<sub>3</sub>O<sub>4</sub>] and/or maghemite [ $\gamma$ -Fe<sub>2</sub>O<sub>3</sub>], with lesser amounts of graphite [C], hematite [ $\alpha$ -Fe<sub>2</sub>O<sub>3</sub>], and only a minute amount of Fe<sup>0</sup> (Figure S1, Supporting Information). It is difficult to distinguish magnetite and maghemite using powder X-ray methods unless conditions are ideal; thus, here the product is simply referred to as magnetite–maghemite. However, the optical microscopic observations showed zoning of magnetite and maghemite. This is consistent with the Raman spectroscopic observations of Ritter et al. (17) in that the oxide films on Fe<sup>0</sup> consist of an inner layer of magnetite, an outer layer of maghemite, and partial rinds of hematite.

On day 405, only the sample from column B was analyzed for mineral identification, with a particular focus on iron

carbonate species. Figure S2 (Supporting Information) shows the X-ray diffractogram of the sample from column B, together with the diffraction peaks identified from the diffraction data for various standards listed by the International Center for Diffraction Data. The lower diffractogram is from the unground sample, and the upper diffractogram is from the grind-and-decant fines obtained the next day. The main diffraction peaks matched best the data for Powder Diffraction File (PDF) 33-0650, which is orthorhombic iron hydroxy carbonate [ $\text{Fe}_2(\text{OH})_2\text{CO}_3$  or  $\text{Fe}^{2+}_{2-x}\text{Fe}^{3+}_x(\text{OH})_{2+x}\text{CO}_3$ ] (18). Other compounds readily identifiable in this sample were aragonite, graphite, magnetite (or magnetite–maghemite), and metallic iron.

In Figure S2, the first peak (at about  $11.8^\circ 2\theta$ ) is assignable to iron hydroxy carbonate, but the position also coincides with the most intense peak for green rust. Green rust has a characteristic bluish green color attributable to the presence of  $\text{Fe}^{2+}$  that, upon exposure to air, is rapidly oxidized (19). Although various Fe oxide or oxyhydroxide alteration products from green rust have been reported (20), a characteristic feature is that the color changes from blue-green to ochreous (21). Throughout the examination, the color of the air-dried sample remained gray, with no observable ochreous discoloration. If green rust had been present, the peak should have disappeared in the diffractogram obtained on the next day (upper diffractogram in Figure S2) because of atmospheric decomposition of the compound. Thus, the absence of a significant change in the intensity of the  $11.8^\circ$  peak indicated that green rust was not present.

For samples collected on day 541, mineral identification was conducted for the unground samples from all columns. Even though the X-ray peaks were not well-resolved because of the poor quality of the diffracting surface of the X-ray mounts, it was nonetheless possible to identify the major compounds in the samples. Green rust was present only in column A, and iron hydroxy carbonate was the primary compound in the samples from columns B, C, D, and II. The two columns that did not receive dissolved calcium carbonate (columns A and I) formed magnetite–maghemite. The results are summarized in Table S1 of the Supporting Information.

Green rust was identified only in column A. The same sample from column A was rerun 3 h after removal from the anaerobic canister to observe whether changes were detectable. The diffractogram obtained from the initial and subsequent runs are shown in Figure S3 of the Supporting Information. Although the runs were of the same bulk sample, they were not from identical X-ray mounts because it was necessary to use the sample holder for the diffractometry of the other samples. Thus, for the later run, the material was lightly ground in a mortar and a new X-ray mount was prepared. In spite of the concerns about reproducibility, the new X-ray pattern showed convincingly that most of the green rust had disappeared (Figure S3).

For the samples collected on day 649, the diffractograms for all columns were obtained with the grind-and-decant method and are shown in Figure S4 of the Supporting Information. The sample from column A, in which green rust was detected from the previous unground sample on day 541, was ground immediately prior to X-ray analysis. The elapsed time from the beginning of grinding to the start of collection of the X-ray data was about 12 min. The presence of green rust was confirmed by the X-ray diffractogram (Figure S4), but the unit cell of the green rust identified in column A was slightly smaller than that of the X-ray standard. The diffractograms of the samples from columns B, C, and D were similar, as all had iron hydroxy carbonate as the primary alteration compound. Aragonite was not detected in the grind-and-decant diffractogram of column C, though it was observed in the optical section. The samples from columns B and D contained abundant aragonite. The sample from

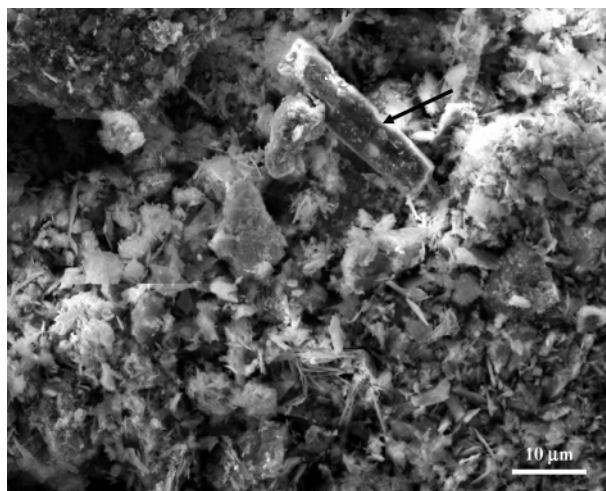


**FIGURE 1.** SEM image of the sample taken from sampling port 6 (at 22.5 cm from the influent end) of column B on day 405. The elongate prismatic grain at the arrow is an aragonite crystal whose width is about  $6\ \mu\text{m}$ . The flakes dispersed throughout the image are iron hydroxy carbonate.

column I consisted mainly of magnetite–maghemite. From the black color of the sample and the absence of a reddish tint, which would be expected from the presence of maghemite, it was concluded that the bulk of the sample was magnetite rather than maghemite. The sample from column II consisted primarily of iron hydroxy carbonate, together with abundant aragonite.

The presence of alteration-derived magnetite–maghemite was uncertain for the samples containing iron hydroxy carbonate because of the overlap with peaks from iron hydroxy carbonate. In all such samples, the proportion of possible magnetite–maghemite was very low, and thus identification was rendered uncertain. Likewise, the presence of iron oxyhydroxides, such as goethite and lepidocrocite, was not identified unequivocally.

**Scanning Electron Microscopy.** *As-Received  $\text{Fe}^0$  and Column A.* The starting  $\text{Fe}^0$  is produced from scrap metals and typically is impure. In the manufacturing process, the scrap is heated in rotary kilns ( $700\text{--}1200^\circ\text{C}$ ) to burn off the nonmetallic materials, especially the cutting oils (17). The heating stage promotes oxidation, and the final product has a rusty appearance because of the presence of surficial iron oxides. The as-received Connelly  $\text{Fe}^0$  had the characteristic rusty appearance, but the surface observed by SEM was not continuously smooth. It included some cavities, defects, cracks, and carbon impurities. Prior to its use as a treatment medium, the  $\text{Fe}^0$  was screened to remove fine particles; thus, some or much of the oxide debris was probably removed by the screening process. The grain size of the  $\text{Fe}^0$  did not appear to have a significant effect on its surface appearance. After the  $\text{Fe}^0$  was used to treat TCE in deionized water, the surfaces of the sample taken from column A were more extensively covered by secondary iron oxides than was the as-received  $\text{Fe}^0$ .

*Columns B, C, and D.* The most abundant secondary solid phases in columns B, C, and D were aragonite and iron hydroxy carbonate. As an example, Figure 1 shows a SEM image of the sample taken from sampling port 6 (at 22.5 cm from the influent end) on day 405 for column B. Aragonite is present as well-formed prismatic crystals, and iron hydroxy carbonate is abundant as minute plates or flakes. Aragonite appeared in many cases as clusters of needle-shaped crystals, as shown in Figure 2 for column D. The needle-shaped aragonite morphology has also been observed by others (2, 3). The presence of flake-like iron hydroxy carbonate has not

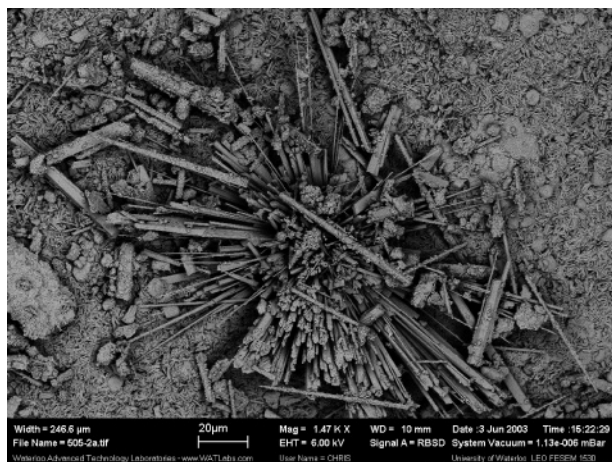


**FIGURE 2.** SEM image of the sample taken from sampling port 2 (at 6.25 cm from the influent end) of column D on day 250. Aragonite is the most dominant secondary precipitate in column D, and it appears as clusters of needle-shaped crystals.

often been reported in the literature (6), but was confirmed by XRD analysis. Calcite was observed in a trace amount (as crystals  $\sim 1 \mu\text{m}$ ) only in column B. Aragonite and calcite have similar solubilities at most temperatures, but the difference in local pH can result in different calcium-carbonate polymorphs. It is also known that divalent cations, such as  $\text{Fe}^{2+}$ , block precipitation sites on nucleating calcite surfaces and promote the development of metastable polymorphs (22).

The importance of high-energy sites, such as grain boundaries, kinks, and surface imperfections, in corrosion of metals has been reported (23). Aragonite precipitated preferentially on the surfaces that had high surface energy, such as at the edges of the iron grains (see Figure S5, Supporting Information). Comparing the two columns receiving the identical feed solution (columns B and C), the crystal sizes in column C were larger than those in column B, probably because larger pore spaces were available for crystal growth in column C. A typical size of aragonite crystals in column B was  $30\text{--}50 \mu\text{m}$  in length and  $3\text{--}6 \mu\text{m}$  in width, whereas that in column C was  $\sim 100 \mu\text{m}$  in length and  $\sim 10 \mu\text{m}$  in width. Column C was, however, observed to have less aragonite than column B, probably because of less iron corrosion resulting from the lower surface area.

Column D had much more aragonite than columns B and C, whereas columns B and C had more iron hydroxy carbonate than aragonite. This is consistent with reports that calcium carbonate precipitation is dominant in high-carbonate waters, in contrast to no significant calcium carbonate precipitation in low-carbonate waters (3). The greater accumulation of aragonite in column D provides an explanation for the rapid migration of the TCE profiles relative to those in columns B and C (13).

A spatial difference in the carbonate-mineral assemblage was apparent for these columns. On day 250, more aragonite was observed at the sampling port close to the influent end than in the ports close to the effluent end, at which more iron hydroxy carbonate was observed. Thus, the bulk of the Ca uptake from the feed solution was precipitated as aragonite in the region closer to the influent end. Dissolved Fe and hydroxide ions were ubiquitous throughout the column; consequently, iron hydroxy carbonate was favored in the region close to the effluent end, a position at which most of the dissolved Ca was no longer available.

**Columns I and II.** Chromium was sequestered mostly in secondary iron oxides in these columns, and the distribution of Cr was highly heterogeneous. Pratt et al. (24) also observed a highly heterogeneous distribution of Cr on granular  $\text{Fe}^0$

used for the removal of chromate. They showed that the reacted  $\text{Fe}^0$  developed coatings of goethite in which Cr occurred only as Cr(III) and was concentrated in the outermost edges. In the current study, temporal and spatial variation in Cr sequestration was obvious. For example, for sampling port 10 (at 42.5 cm from the influent end), Cr was not yet detectable at day 250 because the precipitation front of Fe(III)-Cr(III) (oxy)hydroxide had not yet reached that location.

Aragonite and iron hydroxy carbonate in column II were as abundant as in column D, because they received the same amount of dissolved calcium carbonate. A typical grain size of aragonite in column II was  $30\text{--}40 \mu\text{m}$  in length and  $5\text{--}10 \mu\text{m}$  in width. Generally, the port close to the effluent end had larger- and better-formed crystals than the port close to the influent end. In the region close to the influent end, carbonate minerals were associated with Fe(III)-Cr(III) (oxy)hydroxide. Chromium for column II was sequestered in secondary iron oxides, and in trace amounts in crystal aggregates of iron hydroxy carbonate associated with aragonite.

**Optical Microscopy.** *As-Received  $\text{Fe}^0$  and Column A.* Reflected-light microscopic examination of the as-received sample of  $\text{Fe}^0$  showed that it is heterogeneous with respect to the distribution of iron oxides. All of the particles contained graphite, which occurred in two forms (spherical to lensoid particles and threadlike or sinuous veinlets) and in highly variable amounts. Whereas the spherical-type graphite was more or less homogeneous, most of the sinuous veinlets were heterogeneous, consisting partly of graphite and partly of iron oxides. The volumetric bulk of the magnetite-maghemite occurred as discrete particles or as thin to thick rims on a few  $\text{Fe}^0$  particles. Many of the  $\text{Fe}^0$  particles appeared to be oxide-free at low optical magnifications, but at high magnifications many of the edges had sporadic oxide occurrences and associated oxide debris.

The bulk of the alteration of the  $\text{Fe}^0$  in column A consisted of rims and penetrations by heterogeneous, opaque iron oxides that appeared to be mainly maghemite and are probably complex mixtures of maghemite and magnetite. The outermost rim of the oxide-altered  $\text{Fe}^0$  particles was translucent and consisted of the (former) green rust. Microscopic focusing downward along the interface between the particle exteriors and the mounting medium indicated that the green rust rims were continuous and formed an exterior coating on the  $\text{Fe}^0$  particles.

**Columns B, C, and D.** The primary reaction products in these columns were iron hydroxy carbonate and aragonite. Iron hydroxy carbonate was translucent, and aggregates had a reddish internal reflection. The individual crystals of iron hydroxy carbonate were fibrous (Figure 3), which is an appropriate morphology if the carbonate has a crystal structure related to that of malachite  $[\text{Cu}_2\text{CO}_3(\text{OH})_2]$ . The extent of penetrative replacement and rim development on  $\text{Fe}^0$  was variable from particle to particle. A few particles of  $\text{Fe}^0$  showed that formation of iron hydroxy carbonate was preceded by formation of magnetite-maghemite.  $\text{Fe}^0$  was replaced by iron hydroxy carbonate which, in turn, was overlain by aragonite, thereby providing at least a partial armoring effect (Figure 4). Aragonite was also observed to cement groups of  $\text{Fe}^0$  particles into compact aggregates. A trace amount of calcite, recognizable by its rhombohedral cleavage, was only observed in column C. The presence of calcite in the diffractograms could not be confirmed.

**Columns I and II.** The major alteration product in column I was magnetite-maghemite. EDS analyses to determine whether alteration-derived magnetite-maghemite could be a sink for Cr gave a highly heterogeneous distribution in which Cr content varied from spot to spot. Although the consistent presence of Mn raised the question of whether the Cr in the alteration products was derived from the  $\text{Fe}^0$

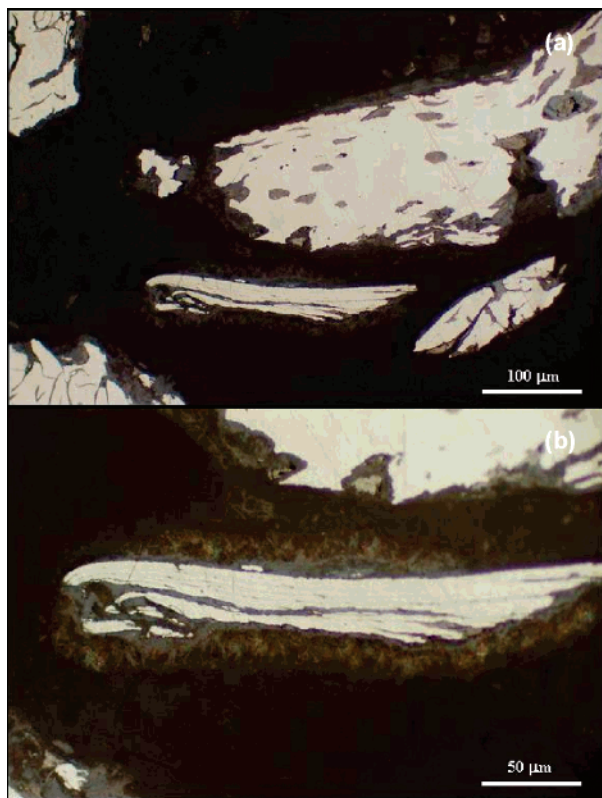


**FIGURE 3.** The sample from column B in plain reflected light. In the upper photo (a), the main  $\text{Fe}^0$  particle contains elliptical pods of graphite and is rimmed by dark gray and bluish gray iron hydroxy carbonate. The lower photo (b), an enlargement of part of the upper photo (a), shows the fibrous form of the iron hydroxy carbonate.

or from the aqueous input containing dissolved Cr(VI), no Cr was detected in any of the spectra of the  $\text{Fe}^0$ .

The sample from column II was optically observed to contain major amounts of iron hydroxy carbonate and aragonite (see Figure S6, Supporting Information). EDS analyses of the aragonite did not show the presence of Cr, but small amounts of Cr were variably sequestered by the iron hydroxy carbonate. Four EDS analyses of iron hydroxy carbonate, in the area shown in Figure S6, indicated the presence of trace amounts of  $\text{Si} > \text{Ca} > \text{Al}, \text{Mn}$ ; two of the spots had traces of Cr. Iron hydroxy carbonate is a mixed-valence compound in which ferrous Fe is predominant, but a small amount of ferric Fe can also be present (6); thus, trace amounts of substitution of  $\text{Cr}^{3+}$  for  $\text{Fe}^{3+}$  is plausible.

**Environmental Significance.** This study examined the reaction products of TCE and Cr(VI) on granular  $\text{Fe}^0$  in solutions containing differing amounts of dissolved calcium carbonate. The reaction products were primarily a consequence of the inorganic chemistry in the feed solutions. The difference in contaminants (TCE vs Cr(VI)) was identifiable only by the additional precipitation of Fe(III)-Cr(III) (oxy)-hydroxide in the columns that received Cr(VI). The spatial and temporal differences in mineral assemblage were governed by the availability of Ca, carbonate, Cr, and dissolved Fe, as the fronts of mineral precipitation migrated along the columns over time.

Aragonite was deposited on iron hydroxy carbonate, partly inhibiting the access of contaminants to the  $\text{Fe}^0$  surfaces. Aragonite also acted as a cementing material between groups of  $\text{Fe}^0$  particles. Thus, aragonite is believed to affect greatly the performance of  $\text{Fe}^0$  in terms of both reactivity and permeability.

Iron hydroxy carbonate was previously reported as a component of a corrosion scale on steel formed at high

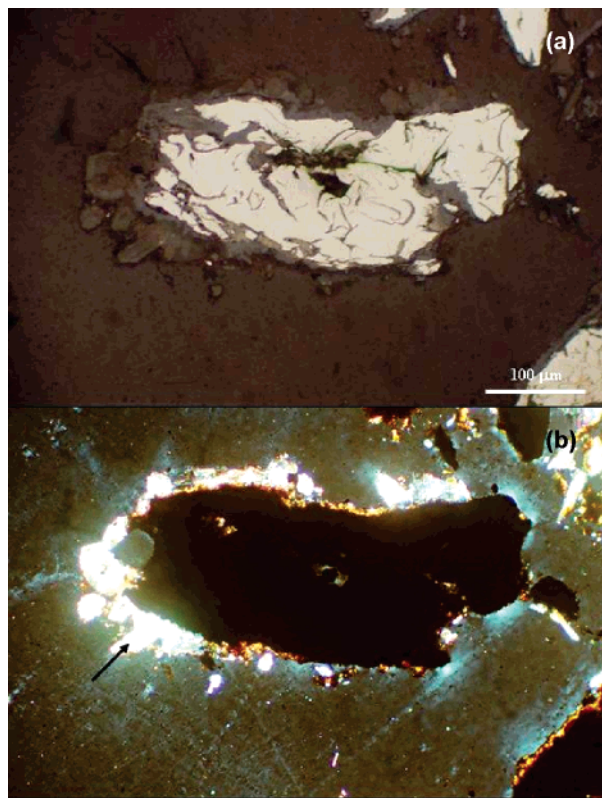


**FIGURE 4.** (a) The sample from column D in plain reflected light and (b) in transmitted light with crossed polarizers. The gray replacement of  $\text{Fe}^0$  is iron hydroxy carbonate, and the exterior is aragonite (bright multicolored grains (arrow) in the lower photo (b)).

temperature and pressure (18) and as a transformation product of biogenic magnetite (25). As reaction products of  $\text{Fe}^0$ , only brief reports are available (7–9). This study investigated this compound in detail, using SEM-EDS, XRD, and optical microscopy. The XRD analyses of material from the columns receiving dissolved calcium carbonate confirmed the presence of iron hydroxy carbonate, which has not yet been reported to occur as a mineral. The compound had a fibrous or flake-shaped morphology, it mostly replaced the edges of the  $\text{Fe}^0$  particles, and it showed some ability to sequester Cr, apparently by substitution of  $\text{Cr}^{3+}$  for  $\text{Fe}^{3+}$ .

Whereas the properties of iron hydroxy carbonate have rarely been mentioned, in a recent study by Kohn et al. (6) it was postulated that the compound may be a redox-active phase which acts as a conductor for electrons between the  $\text{Fe}^0$  core and the contaminants, and that the thickness of the overlayer between the interfacial region and the  $\text{Fe}^0$  core may play an important role in the rate of electron transfer. Because iron hydroxy carbonate apparently may contain a small amount of  $\text{Fe}^{3+}$ , it is speculated that its role in the reaction with contaminants may be similar to that of mixed-valence Fe-bearing minerals; i.e., green rust and magnetite have been shown to be capable of reducing redox-active chemicals (26, 27). The properties of iron hydroxy carbonate and its relationship to phases such as carbonate green rust need to be further investigated because iron hydroxy carbonate may play an important role in governing the performance of  $\text{Fe}^0$  PRBs.

### Acknowledgments

Funding for this research was provided from a Canadian Water Network grant held by D.W. Blowes and from the NSERC/DuPont/EnviroMetal Industrial Research Chair held by R.W. Gillham. Additional funding for S.-W. Jeon was

provided by the Korean Government Scholarship Program. We thank Greg Friday and Wayne Noble of the University of Waterloo, and M. Raudsepp of the University of British Columbia for technical assistance.

### Supporting Information Available

Table of interpretation of the X-ray diffractograms; X-ray diffractograms of the as-received iron and the samples from the columns; SEM image of the sample from column C; microscopic photo of the sample from column II. This material is available free of charge via the Internet at <http://pubs.acs.org>.

### Literature Cited

- (1) Liang, L.; Korte, N.; Gu, B.; Puls, R.; Reeter, C. Geochemical and microbial reactions affecting the long-term performance of in situ 'iron barriers'. *Adv. Environ. Res.* **2000**, *4*, 273–286.
- (2) Phillips, D. H.; Gu, B.; Watson, D. B.; Roh, Y.; Liang, L.; Lee, S. Y. Performance evaluation of a zerovalent iron reactive barrier: mineralogical characteristics. *Environ. Sci. Technol.* **2000**, *34*, 4169–4176.
- (3) Mackenzie, P. D.; Horney, D. P.; Sivavec, T. M. Mineral precipitation and porosity losses in granular iron columns. *J. Hazard. Mater.* **1999**, *68*, 1–17.
- (4) Zhang, Y.; Gillham, R. W. Effects of gas generation and precipitates on performance of Fe<sup>0</sup> PRBs. *Ground Water* **2005**, *43*, 113–121.
- (5) Agrawal, A.; Ferguson, W. J.; Gardner, B. O.; Christ, J. A.; Bandstra, J. Z.; Tratnyek, P. G. Effects of carbonate species on the kinetics of dechlorination of 1,1,1-trichloroethane by zero-valent iron. *Environ. Sci. Technol.* **2002**, *36*, 4326–4333.
- (6) Kohn, T.; Livi, K. J. T.; Roberts, A. L.; Vikesland, P. J. Longevity of granular iron in groundwater treatment processes: corrosion product development. *Environ. Sci. Technol.* **2005**, *39*, 2867–2879.
- (7) Klausen, J.; Vikesland, P. J.; Kohn, T.; Burris, D. R.; Ball, W. P.; Roberts, A. L. Longevity of granular iron in groundwater treatment processes: solution composition effects on reduction of organohalides and nitroaromatic compounds. *Environ. Sci. Technol.* **2003**, *37*, 1208–1218.
- (8) Kamolpornwijiit, W.; Liang, L.; Moline, G. R.; Hart, T.; West, O. R. Identification and quantification of mineral precipitation in Fe<sup>0</sup> filings from a column study. *Environ. Sci. Technol.* **2004**, *38*, 5757–5765.
- (9) Wilkin, R. T.; Su, C.; Ford, R. G.; Paul, C. J. Chromium-removal processes during groundwater remediation by a zerovalent iron permeable reactive barrier. *Environ. Sci. Technol.* **2005**, *39*, 4599–4605.
- (10) Mayer, K. U.; Blowes, D. W.; Frind, E. O. Reactive transport modeling of an in situ reactive barrier for the treatment of hexavalent chromium and trichloroethylene in groundwater. *Water Resour. Res.* **2001**, *37*, 3091–3103.
- (11) Liang, L.; Sullivan, A. B.; West, O. R.; Moline, G. R.; Kamolpornwijiit, W. Predicting the precipitation of mineral phases in permeable reactive barriers. *Environ. Eng. Sci.* **2003**, *20*, 635–653.
- (12) Mayer, K. U.; Blowes, D. W. Constraining reactive transport models using mineralogical data. *Geochim. Cosmochim. Acta* **2002**, *66* (Suppl. 1), A496–A496.
- (13) Jeon, S.-W.; Gillham, R. W.; Blowes, D. W. Effects of carbonate precipitates on long-term performance of granular iron for reductive dechlorination of TCE. *Environ. Sci. Technol.* **2006**, *40*, 6432–6437.
- (14) Jeon, S.-W.; Blowes, D. W.; Gillham, R. W. Performance evaluation of granular iron for removing hexavalent chromium under different geochemical conditions. *J. Contam. Hydrol.*, submitted for publication.
- (15) Hansen, H. C. B.; Koch, C. B.; Nancke-Krogh, H.; Borggaard, O. K.; Sørensen, J. Abiotic nitrate reduction to ammonium: key role of green rust. *Environ. Sci. Technol.* **1996**, *30*, 2053–2056.
- (16) Blowes, D. W.; Ptacek, C. J.; Jambor, J. L. In-situ remediation of Cr(VI)-contaminated groundwater using permeable reactive walls: laboratory studies. *Environ. Sci. Technol.* **1997**, *31*, 3348–3357.
- (17) Ritter, K.; Odziemkowski, M. S.; Gillham, R. W. An in situ study of the role of surface films on granular iron in the permeable iron wall technology. *J. Contam. Hydrol.* **2002**, *55*, 87–111.
- (18) Erdős, V. E.; Altorfer, H. Ein dem Malachit ähnliches basisches Eisenkarbonat als Korrosionsprodukt von Stahl. *Werkst. Korros.* **1976**, *27*, 304–312.
- (19) Refait, P.; Génin, J.-M. R. The oxidation of ferrous hydroxide in chloride-containing aqueous media and Pourbaix diagrams of green rust one. *Corros. Sci.* **1993**, *34*, 797–819.
- (20) O'loughlin, E. J.; Kelly, S. D.; Cook, R. E.; Csencsits, R.; Kemner, K. M. Reduction of uranium(VI) by mixed iron(II)/iron(III) hydroxide (green rust): formation of UO<sub>2</sub> nanoparticles. *Environ. Sci. Technol.* **2003**, *37*, 721–727.
- (21) Génin, J.-M. R.; Bourrié, G.; Trolard, F.; Abdelmoula, M.; Jaffrezic, A.; Refait, P.; Maitre, V.; Humbert, B.; Herbillon, A. Thermodynamic equilibria in aqueous suspensions of synthetic and natural Fe(II)-Fe(III) green rusts: occurrences of the mineral in hydromorphic soils. *Environ. Sci. Technol.* **1998**, *32*, 1058–1068.
- (22) Gutjahr, A.; Dabringhaus, H.; Lacmann, R. Studies of the growth and dissolution kinetics of the CaCO<sub>3</sub> polymorphs calcite and aragonite. II. The influence of divalent cation additives on the growth and dissolution rates. *J. Crystal Growth* **1996**, *158*, 310–315.
- (23) Melendres, C. A.; Pankuch, M.; Li, Y. S.; Knight, R. L. Surface enhanced Raman spectroelectrochemical studies of the corrosion films on iron and chromium in aqueous solution environments. *Electrochim. Acta* **1992**, *37*, 2747–2754.
- (24) Pratt, A. R.; Blowes, D. W.; Ptacek, C. J. Products of chromate reduction on proposed subsurface remediation material. *Environ. Sci. Technol.* **1997**, *31*, 2492–2498.
- (25) Kukkadapu, R. K.; Zachara, J. M.; Fredrickson, J. K.; Kennedy, D. W.; Dohnalkova, A. C.; McCready, D. E. Ferrous hydroxy carbonate is a stable transformation product of biogenic magnetite. *Am. Mineral.* **2005**, *90*, 510–515.
- (26) Williams, A. G. B.; Scherer, M. M. Kinetics of Cr(VI) reduction by carbonate green rust. *Environ. Sci. Technol.* **2001**, *35*, 3488–3494.
- (27) Lee, W.; Batchelor, B. Abiotic reductive dechlorination of chlorinated ethylenes by iron-bearing soil minerals. 1. Pyrite and magnetite. *Environ. Sci. Technol.* **2002**, *36*, 5147–5154.

Received for review August 1, 2006. Revised manuscript received December 21, 2006. Accepted December 24, 2006.

ES0618393